Front. Phys. 11(6), 115206 (2016)
DOI 10.1007/s11467-016-0590-5

RESEARCH ARTICLE

Molecular dynamics simulations of microscopic structure of ultra strong shock waves in dense helium

Hao Liu[1,2], Wei Kang[1,2,*], Qi Zhang[3], Yin Zhang[3], Huilin Duan[1,3,†], X. T. He[4,5,‡]

[1] *HEDPS, Center for Applied Physics and Technology, Peking University, Beijing 100871, China*
[2] *College of Engineering, Peking University, Beijing 100871, China*
[3] *Department of Mechanics and Engineering Science, College of Engineering, Peking University, Beijing 100871, China*
[4] *Center for Applied Physics and Technology, HEDPS, and IFSA Collaborative Innovation Center of MoE, Peking University, Beijing 100871, China*
[5] *Institute of Applied Physics and Computational Mathematics, Beijing 100088, China*
*Corresponding authors. E-mail: * weikang@pku.edu.cn, † hlduan@pku.edu.cn, ‡ xthe@iapcm.ac.cn*
Received February 20, 2016; Accepted March 14, 2016

Hydrodynamic properties and structure of strong shock waves in classical dense helium are simulated using non-equilibrium molecular dynamics methods. The shock speed in the simulation reaches 100 km/s and the Mach number is over 250, which are close to the parameters of shock waves in the implosion process of inertial confinement fusion. The simulations show that the high-Mach-number shock waves in dense media have notable differences from weak shock waves or those in dilute gases. These results will provide useful information on the implosion process, especially the structure of strong shock wave front, which remains an open question in hydrodynamic simulations.

Keywords shock structure, high Mach number, dense media

PACS numbers 52.35.Tc, 02.70.Ns

Frontiers of Physics

1 Introduction

Shock waves are of fundamental interest to astrophysics [1–4] and inertial confinement fusion (ICF) [5]. They also play an essential role in the hydrodynamics of compressible turbulences [6–10]. It has been well recognized that flow variables, such as density, velocity, temperature, and pressure, undergo a sharp transition in a small region at the vicinity of the shock front. This transition can also induce a number of physical or chemical changes inside the media [11–14], e.g., shock-induced phase transitions, shock-induced reactions, molecular dissociation, and atomic ionization, which are of great importance to scientific and engineering applications [11–14]. It is therefore highly desirable to have insight into the microscopic structure of shock waves with atomic resolution, especially the structure near the shock front, as far as the implosion process of ICF experiments is concerned [5]. Investigations of the shock wave structure using the hydrodynamic equations are restrained by the underlying assumption of local equilibrium for flow variables, which is not valid under the highly non-equilibrated conditions at the vicinity of the shock front, and therefore cannot provide a satisfactory description of the shock structure [15–19]. The limit of the local equilibrium assumption can be removed either by the kinetic method [20] or by the non-equilibrium molecular dynamics (NEMD) method [21]. The former is based on the Boltzmann equation [20, 22]. Since the reliability of the method strongly depends on the accuracy of the approximation to the collision integration, it is usually limited to the application of shock waves in gases of low density. Recent development of the discrete Boltzmann method [23–27] significantly increases the application range of the kinetic method, providing a series of valuable results on strong shock waves. One of the important results from the kinetic method is the so-called bimodal approximation proposed by Mott–Smith [20], where the velocity distribution function $f(\boldsymbol{v}, z)$ near the shock front is approximated as a weighted linear combination of the distributions in the upstream and downstream regions as $f(\boldsymbol{v}, z) = \alpha_f(z) f^{up}(\boldsymbol{v}) + [1 - \alpha_f(z)] f^{down}(\boldsymbol{v})$. Here f^{up} and f^{down} are Maxwellian distribution functions in the upstream and downstream regions respectively, and $\alpha_f(z)$ is a position-dependent weight function. A series of analytical studies based on the bimodal model has been carried out on shock waves [28, 29]. Comparison

with other kinetic theories for gas media of low density [22, 30] showed that it worked reasonably well. Alternatively, it is also possible to study the shock waves using the NEMD method [31]. It removes limits from both the local equilibrium assumption and low density media, and can thus be applied to high energy density conditions comparable to those in ICF experiments, where detailed information of the shock wave structure is not easy to probe directly [32–35]. Since the first NEMD simulation of shock waves carried out by Klimenko and Dremin [36] in the late 1970s, major progress on shock wave structures has been made by Hoover *et al.* [37, 38], Holian *et al.* [17–19, 39], and Zhakhovskii [21] using the NEMD method. Their results revealed the insufficiency of the hydrodynamic method in the highly non-equilibrium region near the shock wave front. Based on their results, a number of models [17–19, 40–42] have been proposed to correct the hydrodynamic theories of shock wave structure.

In this work, we present a systematic NEMD simulation of strong shock waves in dense helium, focusing on the shock velocity range from 8 km/s to 130 km/s. The corresponding Mach number range is from 5 to 250. In order to get a shock wave without any influence of ionization, molecular dissociation, or radiation, a classical helium system is chosen as the propagating medium for the shock wave. By doing this, one can expect to have a strong shock wave simply mechanically originated, which can then serve as the reference for further investigations of shock-induced ionization and reaction. With the NEMD simulation, we show that (i) the hydrodynamic properties of high-Mach-number shocks approach to those of strong shocks in mono-atomic ideal gases; (ii) the profile of hydrodynamic quantities, such as ρ, P, and T, in the propagating direction of the shock are not synchronized to each other near the shock front; (iii) at high Mach number, the velocity distribution displays considerable discrepancy from the bimodal approximation; (iv) the inhomogeneity of the thermal energy at the shock front, defined as $\alpha_T = T_{//}^{max}/T_p$, is approximately a constant, where $T_{//}^{max}$ is the maximum effective temperature parallel to the propagating direction, and T_p is the downstream particle temperature; (v) although the Fourier's law is not valid near the shock front, a modified formula $J_z = -\kappa \mathrm{d}T_\perp/\mathrm{d}z$ is able to describe the heat flux J_z in the propagating direction with good accuracy; and (vi) the thickness of the shock front δ can be described using a modified Muckenfuss's formula [29] as a function of the Mach number. The rest of the article is organized as follows. Details of the simulation and the calculation of hydrodynamic quantities are given in Section 2. Main results of the NEMD simulations and corresponding analyses are presented in Section 3. The article is concluded with a short summary in Section 4.

2 Details of the NEMD simulations

The propagation of shock waves in dense helium is simulated using the NEMD method, assuming that the interaction between atoms (or ions) is classical [43]. This method transforms the integration of the Navier–Stokes (NS) equation to the calculation of a set of Newtonian equations of interacting particles with atomic resolution. The NEMD simulation is performed using the molecular dynamics code `LAMMPS` [44], where the symplectic Verlet algorithm [45] is adopted to forward the time step. In order to have a close comparison with the hydrodynamic theories [39], complicated physical processes such as shock-induced phase transitions, dissociation of molecules, and excitation of electrons during the propagation of the shock waves are duly avoided in the simulation. Two initial states of the helium media are considered. The first one, referred to as Case I hereafter, is $T_0 = 300$ K and $\rho_0 = 0.43$ g/cm^3, at which the number density is set to be the same as that of the DT target in the ICF experiments, and the temperature is higher than the critical point so that no phase transition takes place in the propagating processes. In this case, the dimension of the simulation box, as schematically displayed in Fig. 1(a), is 50 Å× 50 Å× 3000 Å, where 478 400 atoms are included in the simulation. The second initial state, referred to as Case II, is $T_0 = 20$ K and $\rho_0 = 0.12$ g/cm^3. The density is taken from the shock experiments conducted by Nellis *et al.* [46], and the temperature is set to be above the boiling point (4.222 K) of helium to avoid phase transitions. In this case, the dimension of the simulation zone is 113 Å× 113 Å× 3777 Å, and over 900 000 atoms are used to simulate the shock wave.

In both cases, the shock propagates along the long edge of the simulation box, which is denoted as the z axis. At one end along the z axis, a piston consisting of several layers of rigid atoms is applied to the helium medium with a constant velocity v_p. The piston is similar to the one used in Ref. [47]. At the other end, the medium is terminated with a reflective boundary. In the directions perpendicular to the propagation of the shock wave, which are denoted as the x and y axes, periodic boundaries are employed to prevent the finite-size effect of boundary reflections. The time step Δt in each simulation depends on v_p. Its maximum value to keep the simulation stable can be estimated by the criterion $\Delta t_{max} = (1/40)(3/4\pi n_I)^{1/3}\sqrt{k_B T/m_I}$, where m_I is the mass of each helium ion/atom, and n_I is the number density in the downstream region of the shock wave. Roughly speaking, the Δt_{max} is about 1/80 of the time that a helium ion/atom travels through the average distance between two adjacent particles.

In the NEMD simulation, the well-established Aziz po-

tential [48] is used to describe the pair interaction between helium atoms. It has a form of

$$V(r) = \epsilon V^*(x),$$
$$V^*(x) = A\exp(-\beta x) - \left(\frac{C_6}{x^6} + \frac{C_8}{x^8} + \frac{C_{10}}{x^{10}}\right) F(x), \quad (1)$$

where

$$F(x) = \begin{cases} \exp\left[-\left(\frac{D}{x} - 1\right)^2\right], & \text{for } x < D, \\ 1, & \text{for } x \geq D, \end{cases} \quad (2)$$

$x = r/r_m$, $r_m = 2.9673$ Å, $\epsilon/k_B = 10.8$ K, $A = 0.544\ 850\ 4 \times 10^6$, $\beta = 13.353\ 384$, $C_6 = 1.373\ 241\ 2$, $C_8 = 0.425\ 378\ 5$, $C_{10} = 0.178\ 100$, and $D = 1.241\ 314$. Macroscopic observables that have counterparts in the NS equation are calculated as the spatial average in the small volume surrounding the given coordinates. The volume has a length of Δz in the z direction, and consists of the entire cross-section $L_x \times L_y$ in the x-y plane. The length of Δz varies from 0.5 Å to 5 Å, depending on the Mach number. Following Refs. [49] and [18], the density $\rho(z)$ is calculated as

$$\rho(z) = \frac{N m_I}{L_x L_y \Delta z}, \quad (3)$$

and the velocity field $\boldsymbol{u}(z)$ is

$$\boldsymbol{u}(z) = \frac{1}{N}\sum_{i=1}^{N} \boldsymbol{u}_i, \quad (4)$$

where N is the total number of particles in the small volume Ω, and $\boldsymbol{u}_i$ is the velocity of a particle. Denoting the x, y, and z components of $\boldsymbol{u}$ as u, v, and w, respectively, the temperature $T(z)$, and pressure $P(z)$ are calculated as

$$T(z) = \frac{m_I}{3Nk_B}\sum_{i=1}^{N}\{u_i^2 + v_i^2 + [w_i - w(z)]^2\}, \quad (5)$$

and

$$P(z) = \rho(z)k_B T + \frac{1}{\Omega}\sum_{i\,\text{in}\,\Omega}\sum_{j\neq i} \boldsymbol{f}_{ij}\cdot(\boldsymbol{r}_i - \boldsymbol{r}_j), \quad (6)$$

where $\boldsymbol{f}_{ij}$ is the force between two particles resulting from the pair interaction, and $\boldsymbol{r}_i$ is the displacement of the particles.

At the vicinity of the shock front, where the non-equilibrium effect is significant, the temperature is decomposed into components parallel and perpendicular to the propagating direction as

$$T_{//} = \frac{m_I}{Nk_B}\sum_{i=1}^{N}[w_i - w(z)]^2, \quad (7)$$

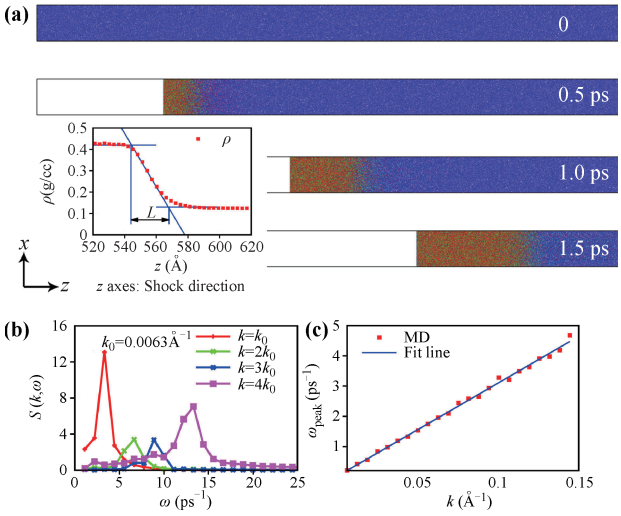

Fig. 1 **(a)** Setup of the NEMD simulations, where shock wave propagates along the z axis. The piston is applied at the left end. The method used to determine the thickness is illustrated in the sublet. **(b)** The profile of $S(\boldsymbol{k},\omega)$ as a function of ω at a series of $\boldsymbol{k}$, where the peak of $S(\boldsymbol{k},\omega)$ takes place at frequencies linearly increased with $\boldsymbol{k}$. **(c)** Dispersion relation of ion acoustic modes in the upstream region used to determine the sound speed c_s. Note that the data in (b) and (c) are taken from the simulations of Case I.

$$T_{\perp} = \frac{m_I}{2Nk_B}\sum_{i=1}^{N}(u_i^2 + v_i^2), \quad (8)$$

to give a detailed account for the non-equilibrium effect. In addition, the average energy of each ion/atom is further decomposed into three contributions as

$$E(z) = E^k(z) + E^{th}(z) + E^{pot}(z), \quad (9)$$

where $E^k(z) = (1/2)m_I|\boldsymbol{u}(z)|^2$ is the kinetic energy corresponding to the macroscopic observable $\boldsymbol{u}(z)$, $E^{th}(z) = (3/2)k_B T$ is the thermal part of the kinetic energy, and $E^{pot}(z)$ is the potential energy defined as $E^{pot}(z) = 1/N\sum_{(i\,\text{in}\,\Omega)}\sum_{j\neq i} V(|\boldsymbol{r}_i - \boldsymbol{r}_j|)/2$. Similar to T, $E^{th}(z)$ can also be decomposed into parallel and perpendicular components with respect to the propagation direction of the shock wave. The heat flux is calculated as [18, 49]

$$Q(z) = \frac{1}{\Delta z L_x L_y}\sum_{i=1}^{N}\left\{\frac{1}{2}m_I[(w_i - w(z))^2 + u_i^2 + v_i^2] + \frac{1}{2}\sum_{j\neq i} V(|\boldsymbol{r}_i - \boldsymbol{r}_j|) + W_i^{zz}\right\}[w_i - w(z)] + \sum_{i=1}^{N}(W_i^{zx}u_i + W_i^{zy}v_i), \quad (10)$$

where $W_i^{\alpha\beta}$ $(\alpha, \beta = x, y, z)$ are internal virial terms defined as

$$W_i^{\alpha\beta} = \frac{1}{2}\sum_{j\neq i}(\boldsymbol{f}_{ij})_\alpha(\boldsymbol{r}_i - \boldsymbol{r}_j)_\beta.$$

The sound speed c_s in the upstream region of the shock wave is determined through the ion-ion dynamic structure factor $S(\boldsymbol{k},\omega)$ [50], which is the Fourier transformation of the correlation function $G(\boldsymbol{r}_1 - \boldsymbol{r}_2, t - t') = \langle n(\boldsymbol{r}_1, t)n(\boldsymbol{r}_2, t')\rangle$, defined as

$$S(\boldsymbol{k},\omega) = \frac{1}{(2\pi)^4}\int_{-\infty}^{\infty} \mathrm{d}\boldsymbol{x}\mathrm{d}\tau G(\boldsymbol{x},\tau)\mathrm{e}^{-\mathrm{i}(\boldsymbol{k}\cdot\boldsymbol{x}-\omega\tau)},$$

with $n(\boldsymbol{r}, t)$ the density of helium at point $\boldsymbol{r}$ and time t. Typical $S(\boldsymbol{k},\omega)$'s are displayed in Fig. 1(c) for selected $\boldsymbol{k}$. At small wave vectors, the maximum value of $S(\boldsymbol{k},\omega)$ takes place at frequencies proportional to $\boldsymbol{k}$. As shown in Fig. 1(c), the proportional factor of ω_{peak} with respect to $|\boldsymbol{k}|$ gives the magnitude of c_s. The Mach number M is then calculated as the ratio of the shock wave speed v_s to the upstream sound speed c_s.

3 Results and discussion

3.1 Hydrodynamic properties of shock waves

A series of shock waves of various v_s is generated in the medium initially at rest, as schematically depicted in Fig. 1(a). The piston has a constant velocity v_p. When the shock wave arrives at its stable state, the downstream particle velocity equals the piston velocity v_p. The sound speed c_s in the unperturbed medium is determined through the $S(\boldsymbol{k},\omega)$, as described in the preceding section. The c_s in Case I is determined to be 3.2 km/s, and it is 0.423 km/s in Case II. Hydrodynamic properties, including the piston velocity v_p, shock velocity v_s, Mach number M, compression ratio η and the thickness of shock front δ are summarized in Table 1. Note that the v_s in both media covers a large range from ~ 8 km/s, which is the upper limit of light gas gun experiments [51], to above 100 km/s, which reaches the lower bound of the Laser-driven compression experiments [52, 53]. The Mach number of the shock waves varies from 4.7 to 252.17.

It is observed that the hydrodynamic properties in the upstream and downstream of the shock front are similar to those of strong shock waves in mono-atomic ideal gases. For example, Fig. 3 shows that the shock speed v_s is proportional to the piston speed v_p downstream. Also, there is a linear relationship between the temperature of downstream materials and the square of v_p, as displayed in Fig. 2. These two properties can be obtained analytically for mono-atomic ideal gases [54, 55]. Following Refs. [54] and [55], the energy conservation in the upstream and downstream flows can be expressed in the coordinates moving with the shock front as

$$c_vT_0 + \frac{u_0^2}{2} + \frac{p_0}{\rho_0} = c_vT_1 + \frac{u_1^2}{2} + \frac{p_1}{\rho_1}, \tag{11}$$

where c_v is the specific heat at constant volume, u is the velocity of flows with respect to the shock front, p is the pressure, and ρ is the density. The subscripts 0 and 1 stand for the upstream and the downstream flows respectively. Combined with the equation of state for ideal gases,

$$c_vT = \frac{p}{\rho(\gamma - 1)}, \tag{12}$$

and the mass conservation law of shock waves

Table 1 Shock wave parameters calculated from the NEMD simulations, where v_p is the piston velocity, c_s is the sound speed in the media, v_s is the shock wave speed, M is the Mach number, η is the compress ratio, and δ is the thickness of the shock front measured from the density profile. Two initial medium conditions are denoted with I and II.

	v_p (km/s)	c_s (km/s)	v_s (km/s)	M	η	δ (Å)
I	9	3.2	15.7	4.7	2.35	5
	30	3.2	43.2	13.0	3.28	10
	40	3.2	56.0	17.0	3.49	14
	50	3.2	69.0	21.1	3.63	23
	60	3.2	82.0	25	3.70	30
	75	3.2	101.9	31.3	3.79	43
	90	3.2	121.5	37.5	3.86	65
	100	3.2	134.7	41.7	3.88	87
II	5	0.423	7.77	18.37	2.83	11
	10	0.423	14.66	34.66	3.17	14
	20	0.423	28.23	66.74	3.5	22
	40	0.423	54.43	128.68	3.83	52
	80	0.423	106.67	252.17	4.17	132

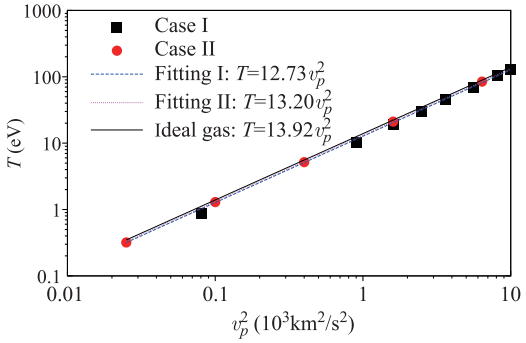

Fig. 2 The downstream temperature T plotted with respect to v_p^2. Red circles and black cubes are downstream temperatures measured in the NEMD simulations. The blue and pink dashed lines are linear fitting curves of the measured temperature, and the black line is the theoretical result for an ideal gas, which shows that $T \propto v_p^2$.

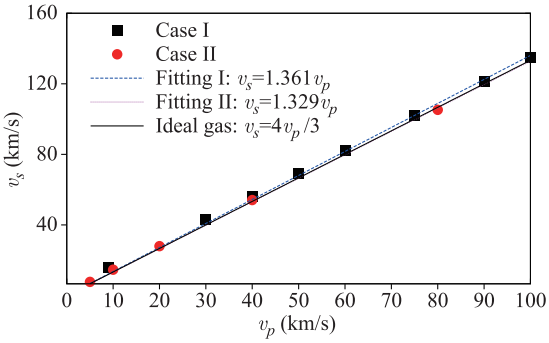

Fig. 3 Relation between the shock wave velocity v_s and the piston velocity v_p. Black cubes and red circles are measured from the NEMD simulations, blue and pink dashed lines are linear fitting curves of the NEMD results, and the black line is the theoretical prediction of strong shock waves in mono-atomic ideal gases.

$$\rho_0 u_0 = \rho_1 u_1, \tag{13}$$

one gets

$$u_0 = \frac{\gamma+1}{4}(u_0-u_1) + \sqrt{c_s^2 + (\frac{\gamma+1}{4})^2 (u_0-u_1)^2}, \tag{14}$$

and

$$T_1 - T_0 = \frac{u_0^2 - u_1^2}{2c_v\gamma}, \tag{15}$$

where γ is the isentropic exponent, $u_0 = v_s$ and $u_1 = v_s - v_p$. When taking the strong shock wave limit, Eq. (14) approaches to

$$v_s = \frac{\gamma+1}{2} v_p, \tag{16}$$

and Eq. (15) is simplified as

$$T_p = T_1 = T_0 + \frac{v_p^2}{2c_v} \approx \frac{v_p^2}{2c_v}. \tag{17}$$

Note that v_s, v_p, and T_p are quantities in the laboratory reference frame. Figure 3 displays the v_s as a function of v_p, directly measured from the simulations. From Fig. 3, the proportional coefficient between v_s and v_p is determined to be 1.33, which implies that $\gamma \approx 1.67$. One can also plot T_p with respect to v_p^2, as displayed in Fig. 2, where the slope of the curves suggests that $1/(2c_v) \approx 13.0$ km^2/(s^2·eV). Both are close to the values of mono-atomic ideal gases, where $\gamma = 5/3$ and $1/(2c_v) = 13.92$ (km^2·s^{-2}·eV^{-1}). These results suggest that the hydrodynamic behavior of these strong shock waves is similar to that of those in mono-atomic ideal gases, which is quite surprising at first glance, considering that the helium has a high density and the interaction between atoms/ions is strong. A decomposition of the total energy per atom/ion at $\rho = 0.43$ g/cm^3 and $T = 300$ K shows that the ratio of $E^{th}/E^p = 1.35$. In the other case, the ratio is 1.25. Both show that the media are far from ideal gases.

3.2 Profiles for flow variables near the shock wave front

To further illustrate why the simulated strong shock waves are similar to those in ideal gases, we display hydrodynamic quantities in Fig. 4 as a function of the z coordinates in the frame of reference attached to the shock wave front. Unlike in the macroscopic hydrodynamics, where the front of shock waves is treated as a sharp discontinuity, the simulated shock waves have subtle structures, as have been illustrated by previous NEMD studies [21, 22, 30, 32, 37, 39, 42, 56]. At high speed, especially when $M \gg 1$, the hydrodynamic quantities are not synchronized to each other, as shown in Fig. 4. The lack of synchronization is displayed in two aspects. First, the range of the effective temperature transition is slightly larger than that of the density transition, because a small number of high energy particles penetrate into the upstream region of the shock front. These high energy particles lead to a long tail of the temperature profile into the upstream region, as shown in Fig. 4. In the simulation, the transition range is measured graphically as displayed in the sublet of Fig. 1(a). In Case I, the transition range derived from the density profile at $v_p = 100$ km/s is $\sim$ 90 Å, while it is approximately 200 Å when derived from the temperature profile. This suggests that the thermal diffusion length across the shock front is much longer than that of the mass diffusion on average. Second, the middle point of the temperature profile is not coincident with that of the density profile, which has been predicted by the bimodal model of Muckenfuss [29]. As shown in Figs. 4(a)–(d), the temperature profile always has a shift in the upstream direction, which suggests that the particles in the upstream region are heated by the hot particles before the compression. The pressure profiles have less shift from the density profile, as displayed in Figs. 4(e)–(g).

The velocity distribution shows considerable deviation from the prediction of the bimodal model [29] at high Mach number. Figure 5 displays the distribution of the parallel and the perpendicular components of the particle velocity at positions across the shock front. It shows that the velocity distributions of both components display considerable deviations from the model. The peak corresponding to the $f^{up}(\boldsymbol{v})$ is much broader than the model's prediction near the shock front. This is not exactly what was observed by Zhakhovskii *et al.* [21], who showed that the bimodal model worked well at Mach number $\sim$ 4. Figure 6 displays the decomposition of the total energy for each atom. It shows that the ratio of the potential energy E^{pot} to the thermal energy E^{th} keeps

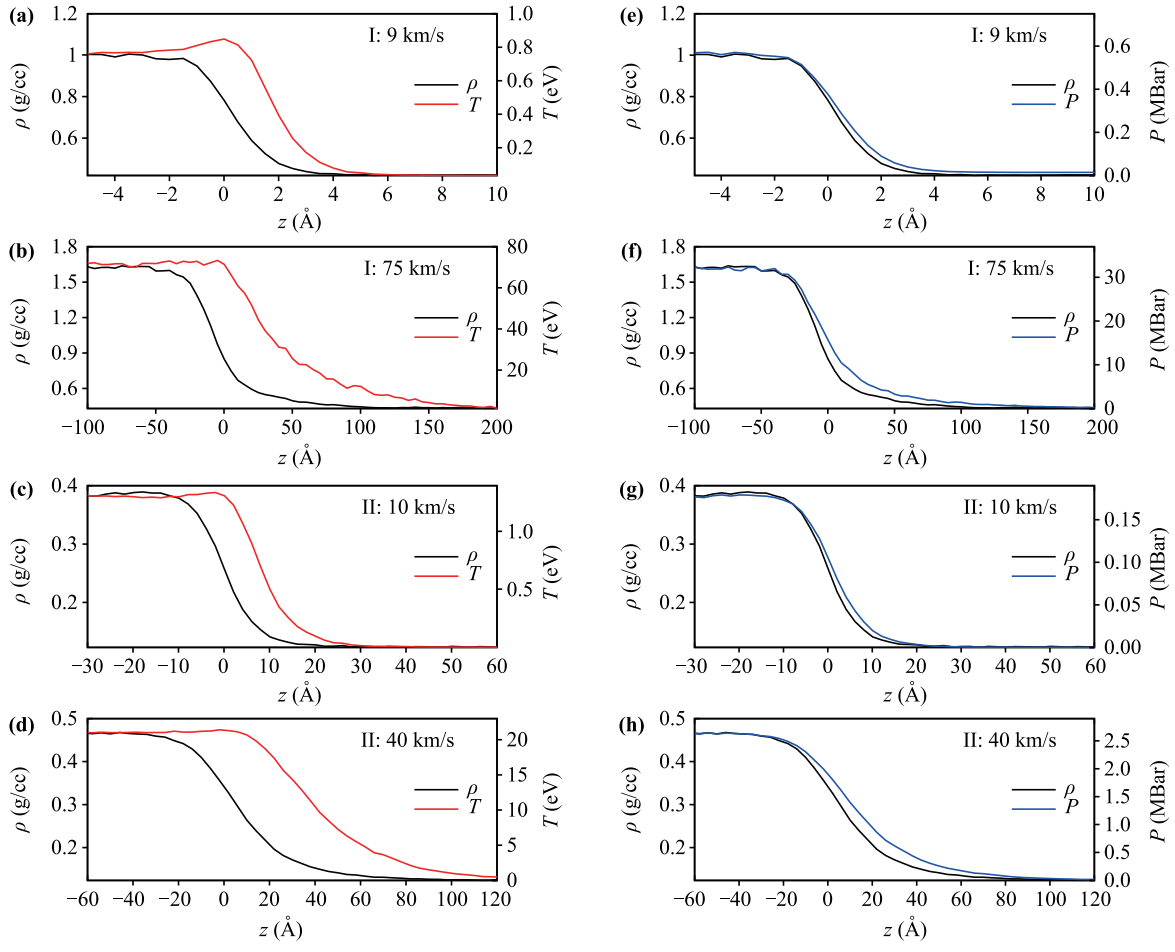

Fig. 4 The profiles of density ρ, temperature T, and pressure P, where **(a)**, **(b)**, **(e)**, and **(f)** correspond to Case I, and **(c)**, **(d)**, **(g)**, and **(h)** correspond to Case II. The profiles of temperature display an upstream shift with respect to the profiles of density, whereas the profiles of pressure follow the profiles of density. The velocity indicated in the figures is the piston velocity v_p.

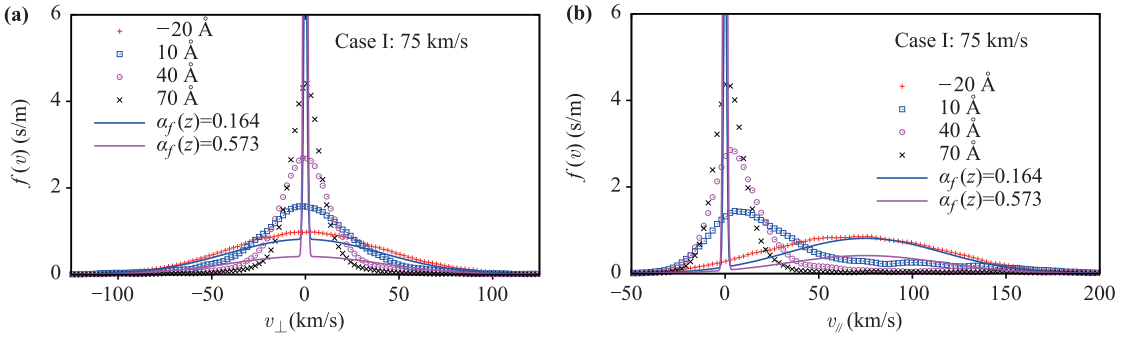

Fig. 5 Velocity distribution of the parallel and the perpendicular components of particle velocity at a series of positions across the shock front in Case I with $v_p = 75$ km/s, where significant deviation from the prediction of the bimodal model is observed. The results of the NEMD simulations are represented by symbols, and the theoretical predictions of the bimodal model are displayed as solid curves.

decreasing with the increase of v_s, whereas the ratio of the kinetic energy E^k to the thermal energy E^{th} approaches 1. The decreasing of E^{pot}/E^{th} comes from the finite compression ratio in a single strong shock compression, which implies that the increase of E^{pot} in the downstream region is finite and most of the energy is in the

forms of kinetic energy and thermal energy. When E^{pot} has a negligible portion in the energy profile, the media will behave like ideal gases. This gives an account for the similarity of the simulated shock waves to those in ideal gases. Fig. 6 also shows that the thermal energy in the transition region is not homogeneously distributed along the perpendicular and parallel directions, which has also been observed in shock waves of small Mach number [17, 21]. $E^{th}_{//}$ has a peak structure and is always larger than $E^{th}_{\perp}$. A quantitative comparison between the peak value of $T_{//}$, denoted as $T^{max}_{//}$, and the average downstream temperature T_p outside the transition region is given in Fig. 7, which shows that the ratio $\alpha_T = T^{max}_{//}/T_p$ is approximately constant, and its value varies between 1.40 and 1.85. Noticing that T is proportional to E^{th}, α_T actually provides a quantitative characterization of the inhomogeneity of the thermal energy, or in another word, the degree of non-equilibrium in the transition region. Figure 8 gives the profile of heat flux in the transition region. Also displayed are the gradients of T and $T_\perp$ with respect to z. It shows that the heat flux is not proportional to $\mathrm{d}T/\mathrm{d}z$ in general, which suggests that the linear Fourier's law of heat conduction is not valid near the shock wave front [38]. This is not surprising since the region is known to be far from equilibrium [17]. Holian came up with a modified heat conduction law with the parallel component of temperature $T_{//}$ rather than T, and achieved a better agreement with the NEMD simulations. However, Fig. 8 shows that the heat flux in this region is approximately proportional to $\mathrm{d}T_\perp/\mathrm{d}z$. In addition, the heat conductivity κ, i.e., the proportionality coefficient, is a constant in the transition region, even the density and temperature vary rapidly in it. For example, for the case displayed in Fig. 8(d), where $v_p = 10$ km/s, $\kappa = 2.0$ J/(m·s·K). In the case displayed in Fig. 8(e), $\kappa = 6.0$ J/(m·s·K). In general, κ increases with the temperature of downstream flow. It is also noticed that the heat flux is not a constant in the transition region, which implies that there is an entropy production process in this region.

3.3 The thickness of shock fronts

The thickness of shock fronts is a key parameter of the shock structure. It was broadly believed since the early work of Becker [57] that the thickness of the shock front δ is on the same order of the mean free path of molecular collisions. The thickness decreases with the pressure difference across the shock front [58] until it was bounded by the diffusion length scale, which is characterized by the mean free path of molecular collisions, at the strong shock wave limit [59]. For the dense helium media, the

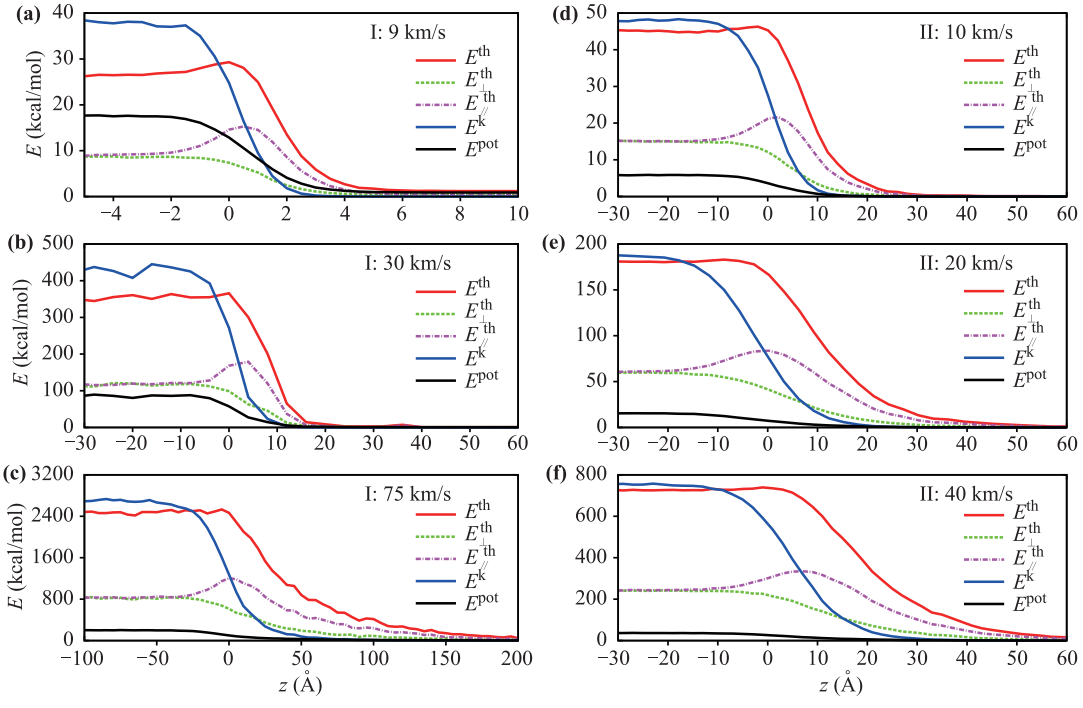

Fig. 6 Profiles of the components for the total energy of each atom, where **(a)**, **(b)**, and **(c)** correspond to Case I, and **(d)**, **(e)**, and **(f)** correspond to Case II. E^{th}, E^k and E^{pot} represent the thermal, kinetic and potential energy of each atom, respectively. $E^{th}_{\perp}$ and $E^{th}_{//}$ are the perpendicular and parallel components of the thermal energy. The velocity displayed in the figures are the piston velocity.

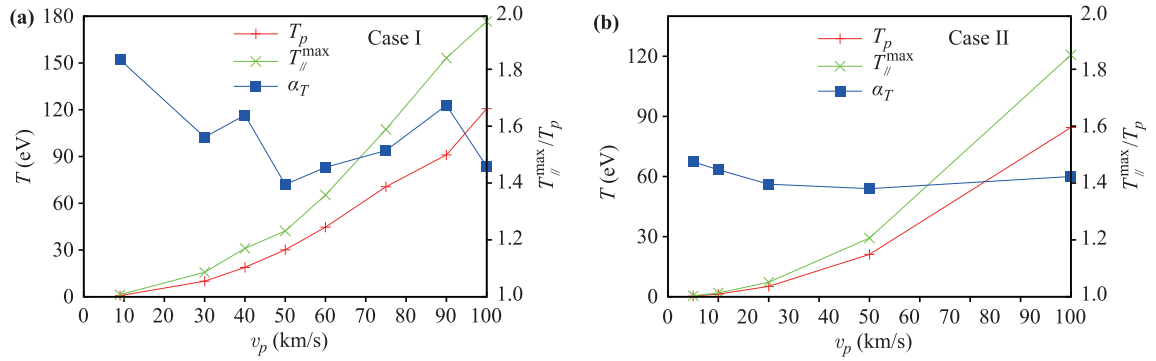

Fig. 7 Comparison of $T_{//}^{max}$ and T_p in the downstream region. The ratio of $T_{//}^{max}/T_p$ is also displayed, which is between 1.4 and 1.8 and insensitive to the change of density and Mach number.

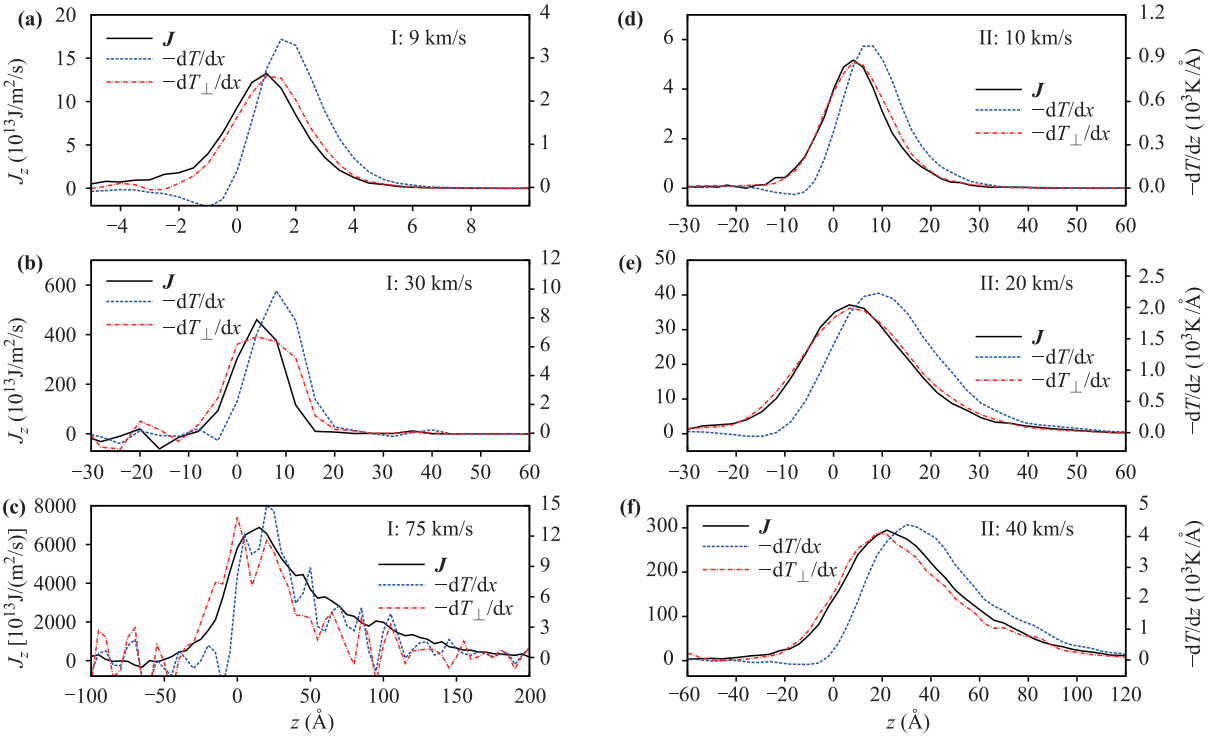

Fig. 8 The profile of the heat flux, where **(a)**, **(b)**, and **(c)** correspond to case I, and **(d)**, **(e)**, and **(f)** correspond to case II. The piston velocity is explicitly denoted in the figure. Also displayed are curves of dT/dz and $dT_\perp/dz$. The figure shows that heat flux is approximately proportional to $dT_\perp$.

hydrodynamic theories [57] predicted a finite $\delta \sim l$ between 1.16 Å and 3.81 Å independent of the Mach number, provided that $l \sim \rho^{-1/3}$ and the compression ratio is ~ 4 at the high Mach number limit [60]. A series of experiments were conducted to determine the thickness δ of shock front using the optical reflectivity method [32–35] for a variety of gases including argon, hydrogen, nitrogen, oxygen, carbon dioxide, and nitrous oxide. It was revealed that the δ in the experiments was considerably larger than the theoretical prediction. Similarly to the experiments, the δ measured in the NEMD simulations grows with the shock speed v_s, as displayed in Fig. 9. Here, the thickness is defined using the density profile following the traditional definition [59], as schematically illustrated in the sublet of Fig. 1(a). A qualitative explanation of the deviation of the theoretical prediction was afforded by Muckenfuss *et al.* [29]. They argued that the high speed particles at the tail of the velocity distribution $f(\boldsymbol{v})$ is the origin of the increasing δ. With the increasing temperature in the downstream region at high Mach number, the number of high speed particles increases, and the penetrating depth of those high speed particles

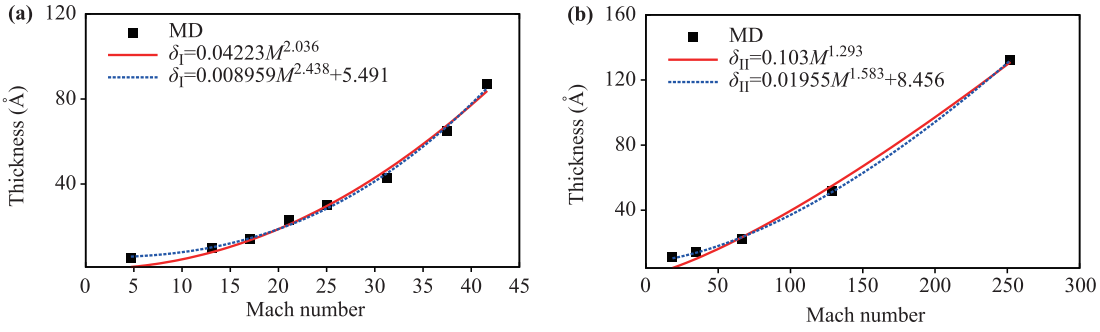

Fig. 9 The thickness of shock fronts plotted with respect to the Mach number. Black cubes are the thickness calculated from NEMD simulation, the pink line is the fitting result of the Muckenfuss model $\delta = a_1 M^{a_2}$, and the blue dashed line is the fitting result of the proposed empirical model $\delta = a_1 M^{a_2} + \delta_0$.

also increases. Based on the bimodal model, they showed that an approximate relation $l/\delta = \alpha_\nu M^{-4/(\nu-1)}$ can be established at the high Mach number limit, where ν and α_ν are parameters determined by the interaction between gas particles, and l is the mean free path of gases.

Here, we propose an empirical formula derived from Muckenfuss [29], which is written as a function of M as

$$\delta = a_1 M^{a_2} + \delta_0,$$

where a_1 and a_2 are two empirical coefficients, and δ_0 gives the thickness at the weak shock limit. In addition to the contribution of the high speed particles in the tail of the distribution function, the empirical formula also takes into consideration the deviation of the distribution function from the bimodal approximation, as is revealed by the NEMD simulations in this work. In the original formula of Muckenfuss, a_2 is a constant determined by the interaction. However, Fig. 9 shows that it also depends on the initial density of the media. For the initial density of $\rho = 0.43$ g/cm^3, $a_2 = 2.438$, and for the initial density $\rho = 0.12$ g/cm^3, $a_2 = 1.5827$. This indicates that further theoretical insight is still required to account for shock waves at extremely high Mach number.

4 Summary

In summary, we have presented a systematic investigation of strong shock waves propagating in classical helium media using the NEMD method. The shock speed in the simulation reaches 130 km/s and the Mach number is over 250, which are close to the parameters of shock waves in the implosion process of ICF. The results will provide useful information to understand the implosion process, especially to illustrate the structure of a high speed shock front, which remains an open question in the hydrodynamic simulations. Based on these results, which are essentially derived from mechanical interactions, the effects of ionization, or chemical reactions on shock waves can then be separated and investigated more thoroughly.

Acknowledgements This work was financially supported by the National Natural Science Foundation of China (NSFC) (Grant No. 11274019) and the National Scholastic Athletics Foundation (NSAF) (Grant No. U1530113).

References

1. A. R. Bell, The acceleration of cosmic rays in shock fronts - I, *Mon. Not. R. Astron. Soc.* 182, 147 (1978)
2. S. J. Schwartz, E. Henley, J. Mitchell, and V. Krasnoselskikh, Electron temperature gradient scale at collisionless shocks, *Phys. Rev. Lett.* 107, 215002 (2011)
3. J. Hansen, M. Edwards, D. Froula, G. Gregori, A. Edens, and T. Ditmire, High Energy Density Laboratory Astrophysics, Chap. Laboratory Simulations of Supernova Shockwave Propagation, Springer Netherlands, Dordrecht, 2005, pp 61–67
4. M. Guidry and B. Messer, The physics and astrophysics of type Ia supernova explosions, *Front. Phys.* 8, 111 (2013)
5. T. J. B. Collins, A. Poludnenko, A. Cunningham, and A. Frank, Shock propagation in deuterium-tritium-saturated foam, *Physics of Plasmas* 12, 062705 (2005)
6. J. Wang, Y. Shi, L.-P. Wang, Z. Xiao, X. He, and S. Chen, Effect of shocklets on the velocity gradients in highly compressible isotropic turbulence, *Physics of Fluids* 23, 125103 (2011)
7. J. Wang, Y. Shi, L.-P. Wang, Z. Xiao, X. T. He, and S. Chen, Effect of compressibility on the small-scale structures in isotropic turbulence, *Journal of Fluid Mechanics* 713, 588 (2012)
8. J. Wang, Y. Shi, L.-P. Wang, Z. Xiao, X. T. He, and S. Chen, Scaling and statistics in three-dimensional compressible turbulence, *Phys. Rev. Lett.* 108, 214505 (2012)

9. D. Rotman, Shock wave effects on a turbulent flow, *Physics of Fluids A: Fluid Dynamics (1989–1993)* 3, 1792 (1991)
10. T. G. Elizarova, A. A. Khokhlov, and S. Montero, Numerical simulation of shock wave structure in nitrogen, *Physics of Fluids (1994–present)* 19, 068102 (2007)
11. B. L. Holian and P. S. Lomdahl, Plasticity induced by shock waves in nonequilibrium molecular-dynamics simulations,*Science* 280, 2085 (1998)
12. A. B. Belonoshko, A. Rosengren, N. V. Skorodumova, S. Bastea, and B. Johansson, Shock wave propagation in dissociating low-z liquids: D2, *J. Chem. Phys.* 122, 124503 (2005)
13. K. Kadau, T. C. Germann, P. S. Lomdahl, and B. L. Holian, Atomistic simulations of shock-induced transformations and their orientation dependence in bcc fe single crystals, *Phys. Rev. B* 72, 064120 (2005)
14. D. W. Brenner, D. H. Robertson, M. L. Elert, and C. T. White, Detonations at nanometer resolution using molecular dynamics, *Phys. Rev. Lett.* 70, 2174 (1993)
15. D. Gilbarg and D. Paolucci, The structure of shock waves in the continuum theory of fluids, *Journal of Rational Mechanics and Analysis* 2, 617 (1953)
16. H. W. Liepmann, R. Narasimha, and M. T. Chahine, Structure of a plane shock layer, *Physics of Fluids* 5, 1313 (1962)
17. B. L. Holian, C. W. Patterson, M. Mareschal, and E. Salomons, Modeling shock waves in an ideal gas: Going beyond the navier-stokes level, *Phys. Rev. E* 47, R24 (1993)
18. B. L. Holian, M. Mareschal, and R. Ravelo, Test of a new heat-flow equation for dense-fluid shock waves, *J. Chem. Phys.* 133, 114502 (2010)
19. B. L. Holian and M. Mareschal, Heat-flow equation motivated by the ideal-gas shock wave, *Phys. Rev. E* 82, 026707 (2010)
20. H. M. Mott-Smith, The solution of the boltzmann equation for a shock wave, *Phys. Rev.* 82, 885 (1951)
21. V. V. Zhakhovskii, K. Nishihara, and S. I. Anisimov, Shock wave structure in dense gases, *Journal of Experimental and Theoretical Physics Letters* 66, 99 (1997)
22. T. Ohwada, Structure of normal shock waves: Direct numerical analysis of the boltzmann equation for hard-sphere molecules, *Physics of Fluids A: Fluid Dynamics (1989–1993)* 5, 217 (1993)
23. A.-G. Xu, G.-C. Zhang, Y.-B. Gan, F. Chen, and X.-J. Yu, Lattice boltzmann modeling and simulation of compressible flows, *Front. Phys.* 7, 582 (2012)
24. Y. Gan, A. Xu, G. Zhang, and Y. Yang, Lattice bgk kinetic model for high-speed compressible flows: Hydrodynamic and nonequilibrium behaviors, *Europhys. Lett.* 103, 24003 (2013)
25. C. Lin, A. Xu, G. Zhang, Y. Li, and S. Succi, Polar-coordinate lattice boltzmann modeling of compressible flows, *Phys. Rev. E* 89, 013307 (2014)
26. A. Xu, C. Lin, G. Zhang, and Y. Li, Multiple-relaxation-time lattice boltzmann kinetic model for combustion, *Phys. Rev. E* 91, 043306 (2015)
27. C. Lin, A. Xu, G. Zhang, and Y. Li, Double-distribution-function discrete boltzmann model for combustion, *Combustion and Flame* 164, 137 (2016)
28. G. G. Comisar, Bimodal distributions and plasma shock wave structure, *Physics of Fluids (1958–1988)* 6, 1263 (1963)
29. C. Muckenfuss, Some aspects of shock structure according to the bimodal model, *Physics of Fluids (1958–1988)* 5, 1325 (1962)
30. G. A. Bird, Aspects of the structure of strong shock waves, *Physics of Fluids (1958–1988)* 13, 1172 (1970)
31. B. Holian, Atomistic computer simulations of shock waves, *Shock Waves* 5, 149 (1995)
32. M. Linzer and D. F. Hornig, Structure of shock fronts in argon and nitrogen, *Physics of Fluids* 6, 1661 (1963)
33. P. Harris and H. N. Presles, Reflectivity of a 5.8 kbar shock front in water, *J. Chem. Phys.* 74, 6864 (1981)
34. G. R. Cowan and D. F. Hornig, The experimental determination of the thickness of a shock front in a gas, *J. Chem. Phys.* 18, 1008 (1950)
35. E. F. Greene and D. F. Hornig, The shape and thickness of shock fronts in argon, hydrogen, nitrogen, and oxygen, *J. Chem. Phys.* 21, 617 (1953)
36. V. Klimenko and A. Dremin, Detonatsiya, Chernogolovka, Akad. Nauk, Moscow, SSSR, 1978
37. W. G. Hoover, Structure of a shock-wave front in a liquid, *Phys. Rev. Lett.* 42, 1531 (1979)
38. W. G. Hoover and C. G. Hoover, Shockwaves and local hydrodynamics; failure of the Navier–Stokes Equations, arXiv: 0909.2882 [physics.flu-dyn]
39. B. L. Holian, W. G. Hoover, B. Moran, and G. K. Straub, Shock-wave structure via nonequilibrium molecular dynamics and Navier–Stokes continuum mechanics, *Phys. Rev. A* 22, 2798 (1980)
40. E. Salomons and M. Mareschal, Usefulness of the burnett description of strong shock waves, *Phys. Rev. Lett.* 69, 269 (1992)
41. L. García-Colín, R. Velasco, and F. Uribe, Beyond the Navier–Stokes equations: Burnett hydrodynamics, *Physics Reports* 465, 149 (2008)
42. A. V. Bobylev, M. Bisi, M. P. Cassinari, and G. Spiga, Shock wave structure for generalized Burnett equations, *Physics of Fluids (1994–present)* 23, 030607 (2011)
43. M. P. Allen and D. J. Tildesley, Computer Simulation of Liquids, Oxford University Press, 1989
44. S. Plimpton, P. Crozier, and A. Thompson, Lammps-large-scale atomic/molecular massively parallel simulator, *Sandia National Laboratories* (2007)
45. L. Verlet, Computer "experiments" on classical fluids. i. thermodynamical properties of lennard-jones molecules, *Phys. Rev.* 159, 98 (1967)

46. W. J. Nellis, N. C. Holmes, A. C. Mitchell, R. J. Trainor, G. K. Governo, M. Ross, and D. A. Young, Shock compression of liquid helium to 56 gpa (560 kbar), *Phys. Rev. Lett.* 53, 1248 (1984)
47. W. Kang, U. Landman, and A. Glezer, Thermal bending of nanojets: Molecular dynamics simulations of an asymmetrically heated nozzle, *Appl. Phys. Lett.* 93, 123116 (2008)
48. R. A. Aziz, V. P. S. Nain, J. S. Carley, W. L. Taylor, and G. T. McConville, An accurate intermolecular potential for helium, *J. Chem. Phys.* 70, 4330 (1979)
49. J. H. Irving and J. G. Kirkwood, The statistical mechanical theory of transport processes (iv): the equations of hydrodynamics, *J. Chem. Phys.* 18, 817 (1950)
50. H. R. Rüter and R. Redmer, *Ab Initio* simulations for the ion-ion structure factor of warm dense aluminum, *Phys. Rev. Lett.* 112, 145007 (2014)
51. B. Lexow, M. Wickert, K. Thoma, F. Schafer, M. H. Poelchau, and T. Kenkmann, The extra-large light-gas gun of the fraunhofer emi: Applications for impact cratering research, *Meteoritics Planetary Science* 48, 3 (2013)
52. Z. Fan, M. Chen, Z. Dai, H.-B. Cai, S.-P. Zhu, W. Zhang, and X. He, A new ignition scheme using hybrid indirect-direct drive for inertial confinement fusion, arXiv: 1303.1252 (2013)
53. H. Shu, X. Huang, J. Ye, J. Wu, G. Jia, Z. Fang, Z. Xie, H. Zhou, and S. Fu, Measuring high pressure equation of state of polystyrene using laser driven shock wave, *Euro. Phys. J. D* 69, 1 (2015)
54. W. Tang, Shock Wave Physics, Science Press, 2011
55. Y. B. Zeldovich and Y. P. Raizer, Physics of Shock Waves and High-Temperature Hydrodynamic Phenomena, Tech. Rep., DTIC Document, 1965
56. V. V. Zhakhovskii, S. V. Zybin, K. Nishihara, and S. I. Anisimov, Shock wave structure in lennard-jones crystal via molecular dynamics, *Phys. Rev. Lett.* 83, 1175 (1999)
57. R. Becker, Stoßwelle und detonation, *Zeitschrift für Physik* 8, 321 (1922)
58. L. Landau and E. M. Lifshitz, Theoretical Physics, Vol. 6, Hydrodynamics, 1986
59. L. H. Thomas, Note on Becker's theory of the shock front, *J. Chem. Phys.* 12, 449 (1944)
60. S. Pfalzner, An Introduction to Inertial Confinement Fusion, CRC Press, 2006